Strain Hardening of Polymer Glasses: Effect of Entanglement Density, Temperature, and Rate

ROBERT S. HOY, MARK O. ROBBINS

Department of Physics and Astronomy, Johns Hopkins University, Baltimore, MD 21218

Received 24 May 2006; revised 28 July 2006; accepted 23 August 2006
DOI: 10.1002/polb.21012
Published online in Wiley InterScience (www.interscience.wiley.com).

ABSTRACT: The strain hardening behavior of model polymer glasses is studied with simulations over a wide range of entanglement densities, temperatures, strain rates, and chain lengths. Entangled polymers deform affinely at scales larger than the entanglement length as assumed in entropic network models of strain hardening. The dependence of strain hardening on strain and entanglement density is also consistent with these models, but the temperature dependence has the opposite trend. The dependence on temperature, rate, and interaction strength can instead be understood as reflecting changes in the flow stress. Microscopic analysis of local rearrangements and the primitive paths between entanglements is used to test models of strain hardening. © 2006 Wiley Periodicals, Inc. J Polym Sci Part B: Polym Phys 44: 3487–3500, 2006

Keywords: compression; computer modeling; glass; mechanical properties; modulus; molecular dynamics; relaxation; rubber; simulations; stiffness; strain hardening

INTRODUCTION

Mechanical deformation of polymer glasses has been studied for many decades, and the basic features of the stress–strain curves are well known.[1] At very small strains the response is elastic. At slightly larger strains, yielding occurs when intermolecular barriers to segmental rearrangements are overcome. Following yield, the material may exhibit strain softening, a reduction in stress to a level corresponding to plastic flow. At higher strains, the stress increases again as the chain molecules orient, in a process known as "strain hardening." The balance of strain softening and strain hardening is critical in determining material properties such as toughness. Polymers that exhibit greater strain hardening, such as polycarbonate, are tougher and tend to undergo ductile rather than brittle deformation, because strain localization is suppressed.

The complex stress–strain behavior of polymer glasses has often been modeled using rubber elasticity theory.[2] Glasses are assumed[3] to behave like a crosslinked rubber, with the number of monomers between crosslinks equal to the entanglement length N_e. The contribution of strain hardening to the stress is then associated with changes in the entropy of the entanglement network under macroscopic deformation. For uniaxial stress with a longitudinal stretch λ, this contribution is given by

$$\sigma(\lambda) = -\lambda T \left(\frac{\partial s}{\partial \lambda}\right)_T, \qquad (1)$$

where $\sigma(\lambda)$ is the true stress, s is the entropy per unit volume, and T is the temperature. In the simplest case, known as "Gaussian" hardening, eq 1 yields $\sigma(\lambda) = G_R(\lambda^2 - 1/\lambda)$, with G_R the "strain hardening" modulus. G_R is predicted to be linearly proportional to both T and the entanglement density ρ_e: $G_R = \rho_e k_B T$.

It is not clear why an entropic argument should apply in the glassy state where chains

Correspondence to: R. S. Hoy (E-mail: robhoy@pha.jhu.edu)

cannot move freely to sample the configurational entropy,[4] but the network model of strain hardening has had much success in describing experimental results on polymer glasses. For example, Gaussian hardening has been observed in many uncrosslinked glasses.[5,6] More recently, van Melick et al. performed experiments[7] that showed G_R has the predicted linear dependence on ρ_e. However, in contrast with the entropic prediction, G_R was not proportional to T but instead decreased linearly with increasing T. Also, G_R was found[7] to be about 100 times larger than $\rho_e k_B T$, even near the glass transition temperature T_g. The higher modulus can be attributed[8] to "frictional forces" or to the greater energy necessary to plastically deform a material below T_g, but quantitatively little is known. Other open questions about glassy strain hardening remain as well, as summarized recently by Kramer.[4]

In this paper we examine the effect of entanglement density, temperature, chain length, and strain rate on the strain hardening behavior of model polymer glasses. Several previous simulation studies have considered strain hardening,[9–14] but none have examined the factors controlling G_R over a wide parameter space. This is desirable to understand the results of van Melick et al. and other recent experiments.[7,15,16] To examine chemistry-independent factors controlling G_R, we use a generic coarse-grained bead-spring model.[17] The lower computational cost of this model allows us to simulate a wide variety of relatively large systems, allowing for good statistics and precise measurements of G_R.

We find that the functional form of the stress–strain curves at fixed temperature and strain rate is consistent with entropic elasticity as defined by eq 1. Both Gaussian hardening and the more dramatic "Langevin" hardening[2] are observed. Moreover, the transition between these two forms is consistent with rubber-elastic predictions.[2] In addition, we reproduce the key result of van Melick et al., $G_R \propto \rho_e$, over a comparable range of entanglement densities.

Other simulation results reveal dramatic inconsistencies with the entropic network model. As in the experiments of van Melick et al.,[7] G_R drops linearly with increasing T. This drop extends to the $T \to 0$ limit, which is clearly inconsistent with eq 1. The ratio of G_R to $\rho_e k_B T$ is also comparable to experiment, remaining of order 100 even near T_g. Our results for the variation of G_R with T, intermolecular interactions, and the rate of deformation can be understood if G_R scales with the plastic flow stress σ_{flow} rather than a network entropy. Indeed entire stress–strain curves at different strain rates and interaction strengths collapse onto a universal curve when scaled by σ_{flow}.

It is known that G_R decreases with decreasing molecular weight, and this has been attributed to greater relaxation of the entanglement network.[15] We study the entire range of molecular weights from the $N \ll N_e$ to $N \gg N_e$ limits, with N the degree of polymerization. We find significant strain hardening even in unentangled systems. At small strains the chains deform affinely, and their increased length and alignment leads to strain hardening that is very similar to that of entangled chains. Only at large strains do the alignment and strain hardening begin to drop below those in entangled systems. The chain length dependence combined with the rate dependence discussed above suggests that strain hardening can be expressed as a product of the flow stress and a factor that represents the amount of local plastic deformation required to maintain connectivity of the chains.

Our simulations also allow us to examine microscopic quantities that are not easily accessible in experiments. Entangled chains deform affinely at large scales, as expected if entanglements act like crosslinks, and there is little entanglement loss through slippage at chain ends. The underlying entanglement structure is studied using primitive path analysis.[18] A primitive path is the shortest path a chain fixed at its ends can take without crossing any other chains.[19] The scaling of primitive path lengths with increasing strain is well described by a model assuming affine stretching of paths, and also by the nonaffine tube model of Rubinstein and Panyukov.[20] The degree of plastic deformation is studied by examining the nonaffine component of deformation at low temperatures. Results for different entanglement densities fall on a universal curve for low strains, but increase more rapidly for higher entanglement densities at large strains. Strain hardening is related to microscopic plastic events, which are required to maintain chain connectivity. As the stress rises with increasing strain, both the number of events and the energy dissipated per event increase.

In the following section we describe the polymer model used in our simulations, and the protocols used to strain the system and identify primitive paths and entanglement lengths.[18] Next we describe the effect of entanglement density, temperature, interaction strength, strain rate, and the

microscopic rearrangements of monomers, chains, and primitive paths. The final section contains conclusions.

POLYMER MODEL AND METHODS

We employ a coarse-grained bead-spring polymer model[17] that incorporates key physical features of linear homopolymers such as covalent backbone bonds, excluded-volume and adhesive interactions, chain stiffness, and the topological restriction that chains may not cross. All monomers have mass m and interact via the truncated and shifted Lennard-Jones potential:

$$U_{\mathrm{LJ}}(r) = 4u_0\left(\left(\left(\frac{a}{r}\right)^{12} - \left(\frac{a}{r_c}\right)^{12}\right) - \left(\left(\frac{a}{r}\right)^{6} - \left(\frac{a}{r_c}\right)^{6}\right)\right), \quad (2)$$

where r_c is the potential cutoff radius and $U_{\mathrm{LJ}}(r) = 0$ for $r > r_c$. Unless noted, $r_c = 1.5a$. We express all quantities in terms of the molecular diameter a, binding energy u_0, and characteristic time $\tau_{\mathrm{LJ}} = \sqrt{ma^2/u_0}$.

Covalent bonds between adjacent monomers on a chain are modeled using the finitely extensible nonlinear elastic (FENE) potential

$$U_{\mathrm{FENE}}(r) = -\frac{kR_0^2}{2}\ln\left(1 - (r/R_0)^2\right), \quad (3)$$

with the canonical parameter choices[17] $R_0 = 1.5a$ and $k = 30u_0/a^2$. N monomers are bound together to make a linear chain, with equilibrium bond length $l_0 \simeq 0.96a$. As a means of varying entanglement density, we introduce chain stiffness using the bending potential

$$U_{\mathrm{bend}}(r) = k_{\mathrm{bend}}(1 - \cos\theta), \quad (4)$$

where θ is the angle betweeen consecutive covalent bond vectors along a chain. Stiffer chains (higher k_{bend}) produce higher entanglement densities, as discussed below.

The values of N employed in this paper range from 4 to 3500, but most simulations have $N = 350$, which is long enough for the systems to be in the highly entangled ($N > 8N_e$) limit. The initial simulation cell is a cube of side length L_0, which is chosen to be greater than the typical end–end distance of the chains. N_{ch} chains are placed in the cell, with periodic boundary conditions applied in all three directions. N_{ch} is chosen so that the total number of monomers $N_{\mathrm{tot}} = NN_{\mathrm{ch}}$ is 30,000–280000, and typically 70000 (Table 1). The monomer number density is $\rho = 0.85a^{-3}$.

Table 1. System Parameters and Values of N_e from PPA

k_{bend}	C_∞	N	N_{tot}	f	N_e
2.0	3.2	350	70,000	0	22
1.5	2.6	350	70,000	0	26
2.0	3.2	350	70,000	0.25	28
2.0	3.2	350	70,000	0.33	29
1.5	2.6	350	70,000	0.25	36
0.75	2.0	350	70,000	0	39
2.0	3.2	350	70,000	0.5	45
0	1.7	500	250,000	0	71
0.75	2.0	350	70,000	0.5	77
0	1.7	3500	280,000	0.5	165

Values of the entanglement length N_e and chain stiffness constant C_∞ are given as a function of k_{bend} and the fraction f of monomers in short chains of five beads. The total number of monomers N_{tot} in the simulation, and length N of long chains are also given.

Each initial chain configuration is a random walk of $N - 1$ steps with the bond angles chosen to give the desired large-scale chain structure

$$C_\infty = \frac{l_K}{l_0} = \frac{1 + \langle\cos(\theta)\rangle}{1 - \langle\cos(\theta)\rangle}, \quad (5)$$

where C_∞ is the chain stiffness constant and l_K is the Kuhn length. In melt studies, C_∞ increases from 1.8 to 3.34 as k_{bend} is increased from 0 to $2.0u_0$.[21] Larger values of k_{bend} produce local nematic order,[22] which is undesirable since we wish to simulate amorphous systems.

After the chains are placed in the cell, we perform molecular dynamics (MD) simulations. Newton's equations of motion are integrated with the velocity-Verlet method[23] and timestep $\delta t = 0.007\tau_{\mathrm{LJ}} - 0.012\tau_{\mathrm{LJ}}$. The system is coupled to a heat bath at temperature T using a Langevin thermostat[24] with damping rate $1.0/\tau_{\mathrm{LJ}}$.

We equilibrate the systems thoroughly at $T = 1.0u_0/k_B$, which is well above the glass transition[25] temperature $T_g \simeq 0.35u_0/k_B$. For short, poorly entangled chains, we use the "fast pushoff" method.[21] The cutoff radius r_c is set to $2^{1/6}a$, as is standard in melt simulations.[17] The chains are allowed to diffuse several times their end–end length before the system is considered equilibrated. For longer chains, the time required for

diffusive equilibration is prohibitively large, so we use the double-bridging-MD hybrid algorithm.[21] In addition to standard MD, Monte Carlo moves that alter the connectivity of chain subsections are periodically performed, allowing the chain configurations to relax far more rapidly.[26] In some cases, to reduce the entanglement density, we cut a fraction f of the long chains into pieces with $N = 5$ after the initial equilibration. Additional MD equilibration is then performed until the newly created short chains have diffused several times their length.

Glassy states are obtained by performing a rapid temperature quench at a cooling rate of $\dot{T} = -2 \times 10^{-3} u_0/k_B\tau_{LJ}$. We increase r_c to its final value and cool at constant density until the pressure is zero. The quench is then continued at zero pressure using a Nose-Hoover barostat.[23] Unless noted, the final temperature is $0.2u_0/k_B$, which is about 3/5 of T_g. This temperature is chosen because it is high enough to observe significant thermal relaxation and strain rate effects, but still well below T_g. The resulting glasses have density $\rho \simeq 1.00a^{-3}$. We have checked that results from other quench protocols are consistent with the conclusions presented below.

To examine trends in G_R with entanglement density, it is necessary to measure $\rho_e = \rho/2N_e$. Melt entanglement lengths have been obtained for undiluted[18] systems and vary from about 70 for fully flexible chains ($k_{bend} = 0$) to 20 for semiflexible chains with $k_{bend} = 2.0u_0$. Measurements have not been made for diluted systems. Also, although quenching a melt into a glass has little effect[27] on N_e, we still measure ρ_e at the various temperatures employed. The changes in ρ_e upon cooling are primarily due to changes in ρ. Values of ρ_e are measured by performing primitive path analyses (PPA)[18,28] on systems with $N \gg N_e$. We also apply PPA to deformed states to examine how the primitive paths evolve with increasing strain.

In PPA, all chain ends are fixed in space and several changes are made to the interaction potential. Intrachain excluded-volume interactions are deactivated, while interchain excluded-volume interactions are retained. Turning off intrachain interactions means that self-entanglements are not preserved, but their number is negligibly small for the systems considered here.[29] The covalent bonds are strengthened by setting $k = 100u_0$, and the bond lengths are capped at $1.2a$ to prevent chains from crossing one another.[29] The FENE potential is linearized for $r < 0.75a$ so the length minimization takes place at constant tension.[28] For semiflexible chains, the bond-bending potential is deactivated by setting $k_{bend} = 0$. For systems diluted with short chains, the short chains are removed. This is justifiable because the short chains' contour length is smaller than the tube diameter.

In the final stage of the PPA the system is coupled to a heat bath at $T = 0.001u_0/k_B$ so that thermal fluctuations are negligible, and the equations of motion are integrated until the chains minimize their length. This typically requires $1000\tau_{LJ}$. Once the chain contour lengths have been minimized, we calculate the primitive path lengths L_{pp}. For undeformed systems, we use the formula given in ref. 18 to calculate the entanglement length:

$$N_e = \frac{\langle R_{ee}^2 \rangle}{L_{pp}^2/(N-1)}, \tag{6}$$

where $\langle R_{ee}^2 \rangle$ is the average squared end–end distance. The primitive paths have Gaussian random walk statistics, with N_e monomers per Kuhn segment.[18,29] Results for different systems are summarized in Table 1.

Several atomistic simulation studies have covered various aspects of strain hardening, but most have been for tensile deformation.[9–12] For fundamental studies of strain hardening, compressive rather than tensile deformation is preferred because it suppresses strain localization. This allows the stress to be measured in uniformly strained systems. Previous atomistic simulations of strain hardening in compression[13,14] used united-atom models of polyethylene, and focused on dihedral (trans/gauche) transition physics rather than quantitative measurement of G_R.

A plurality of the experiments[7,15,16,30,31] most relevant to the present study have employed uniaxial compression; we therefore do the same. The systems are compressed along one direction, z, while maintaining zero stresses along the transverse (x,y) directions.[32] The rapidity of the quench minimizes strain softening, which in turn yields ductile, homogeneous deformation even at the lowest temperatures and highest strains considered here.

The uniaxial stretch λ is defined as L_z/L_z^0, where L_z^0 is the cube side length at the end of the quench. Since we consider compression, λ is less than one. Compression is performed at constant true strain rate $\dot{\varepsilon} = \dot{\lambda}/\lambda$, which is the favored protocol for strain hardening experiments.[8] We use $\dot{\varepsilon}$ of between $-3.16 \cdot 10^{-5}/\tau_{LJ}$ and $-10^{-3}/\tau_{LJ}$. These rates are significantly lower than those employed

in some previous simulations.[11,12] The systems are compressed to true (logarithmic) strains up to $\varepsilon_{\text{final}} = -1.5$, corresponding to $\lambda_{\text{final}} = \exp(-1.5) \simeq 0.223$.

RESULTS

Variation of Stress with Strain and N_e

As noted in the introduction, the entropic network model of strain hardening reproduces the measured variation of stress with strain and N_e. It assumes that the polymer glass acts like a network with chains of N_e beads between crosslinks, and that the stress is proportional to the derivative of entropy with strain (eq 1). Many experiments can be fit to the simplest Gaussian strain hardening model where the chains are assumed to obey Gaussian statistics. For volume-conserving uniaxial compression, the Gaussian strain-hardening model predicts

$$-\sigma = \sigma_0 + G_R g(\lambda), \tag{7}$$

where G_R is the hardening modulus, $g(\lambda) \equiv 1/\lambda - \lambda^2$ describes the functional form of the hardening, and a constant offset σ_0 must be added to fit the initial yield stress. Note that we consider $-\sigma$ so that compression gives positive values in subsequent plots.

The Gaussian approximation breaks down as the root-mean-squared (rms) distance between entanglements $\sqrt{\langle R^2(N_e)\rangle}$ approaches the contour length $N_e l_0$. The "Langevin" hardening model includes the change in configurational entropy as the ratio $h \equiv \sqrt{\langle R^2(N_e)\rangle}/N_e l_0$ increases.[33] For uniaxial compression at constant volume,

$$-\sigma = \sigma_0 + G_R g(\lambda) L^{-1}(h)/3h, \tag{8}$$

where $L^{-1}(x) = 3x + 9x^3/5 + 297x^5/175 + \cdots$ is the inverse Langevin function and $h = \sqrt{(\lambda^2 + 2/\lambda)C_\infty/3N_e}$ for an affine strain.[34] For small h the ratio of Langevin to Gaussian hardening is $1 + 3h^2/5$, and the Gaussian approximation is usually considered adequate[2] for $h < 1/3$.

Figure 1 illustrates how the strain hardening varies with N_e in our simulations. The four cases shown span the range of N_e studied below. All simulations were done at $\dot{\varepsilon} = -10^{-3}/\tau_{\text{LJ}}$, and other parameters are listed in Table 1. As in many experiments,the stress is plotted against $g(\lambda)$ so that Gaussian strain hardening corresponds to a straight line.

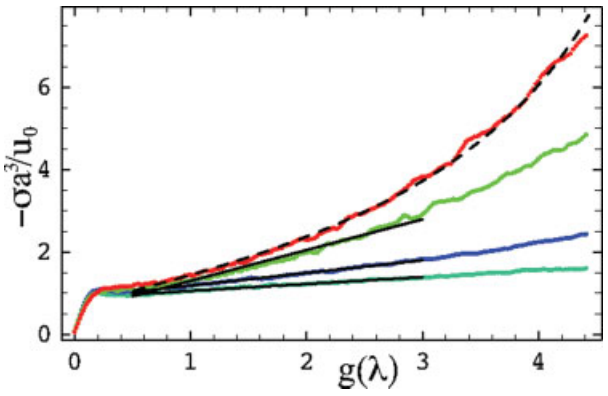

Figure 1. Strain hardening for various degrees of entanglement. The strain rate is $\dot{\varepsilon} = -10^{-3}/\tau_{\text{LJ}}$ and $T = 0.2u_0/k_B$. Successive curves from bottom to top are for $N_e = 165$, $N_e = 71$, $N_e = 26$, and $N_e = 22$ and other parameters are provided in Table 1. Solid black lines indicate linear fits used to determine G_R. A dashed curve shows a fit to eq 8, with the fit value of $N_e = 14.25$. [Color figure can be viewed in the online issue, which is available at www.interscience.wiley.com.]

The behavior at small g is nearly independent of N_e. In this limit, g is proportional to strain. An initial elastic response is followed by yielding at a stress σ_y and nearly ideal plastic flow at a stress σ_{flow}. For the results shown in Figure 1, $\sigma_y \simeq \sigma_{\text{flow}}$, but postyield strain softening occurs at lower temperatures and slower quench rates.

The strain hardening at $g > 0.5$ depends strongly on N_e. For large N_e, the entire curve shows linear Gaussian strain-hardening. As N_e decreases, nonlinear Langevin strain-hardening sets in at smaller g. The nonlinearity becomes pronounced when h exceeds 1/3, as expected from the Langevin expression (eq 8). For $N_e = 22$, $h = 0.4$ in the unstrained state, and the results show pronounced curvature at all g. We find that such strongly nonlinear curves cannot be fit to the Langevin expression unless N_e is taken as a fitting parameter. The quality of such fits is illustrated by the dashed line in Figure 1. The fit value of $N_e = 14.25$ is about 2/3 of the value of $N_e = 22$ obtained from the PPA and plateau modulus.[18]

Experimental fits to Langevin strain hardening also produce smaller entanglement lengths than those determined from the plateau modulus.[30,35] This might be interpreted as a shift in the length between the effective crosslinks produced by entanglements, but may also reflect the limitations of the entropic network model. One is the assumption of constant volume. While volume changes less than 1% for the two systems that

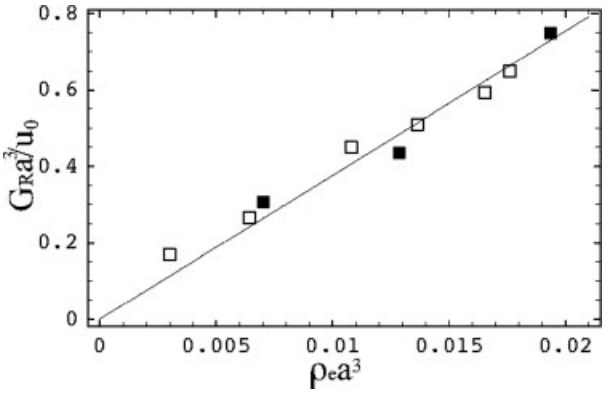

Figure 2. Plot showing proportionality of hardening modulus G_R and entanglement density ρ_e. As shown in Figure 1, G_R is obtained from linear fits for $0.5 \leq g(\lambda) \leq 3$. Filled (empty) squares indicate the undiluted (diluted) systems from Table 1; the fractions f of short chains are indicated in this table. Error bars are of order the symbol size. Results for $N_e = 22$ are not shown since Langevin hardening extends to low strains, but Langevin fits to this and other N_e are consistent with the line drawn through the data.

show Gaussian hardening, systems with $N_e = 26$ and 22 contracted by 3.2 and 5.5% respectively. Much of this contraction occurred at large g and could affect the fit to Langevin hardening.

The network model also predicts that G_R should increase linearly with entanglement density, and this prediction was verified in the recent experimental work of van Melick et al.[7] Following their work, we obtain G_R from linear fits to the stress over the range $0.5 \leq g(\lambda) \leq 3$. Except for the most entangled system, $N_e = 22$, the behavior is nearly Gaussian over this range, and linear and Langevin fits to G_R differ by less than 10%. Results for G_R are plotted against ρ_e in Figure 2 over a slightly wider range ($26 \leq N_e \leq 165$) than considered in the experiments.[7] As predicted by the network model, the results are well fit by a line passing through the origin. In the following sections we will consider whether G_R/ρ_e scales with the temperature or the flow stress. The results in Figure 2 do not distinguish between these interpretations because T is constant and σ_{flow} only varies by $\pm 10\%$.

Some authors have suggested that the Kuhn length l_K, or more properly the chain stiffness constant C_∞, plays a critical role in determining G_R. They argue that the reason that G_R is observed to be higher for polymers with larger C_∞ is that straight chains are harder to deform.[8,9] However, these tests were performed on undiluted systems, in which C_∞ and ρ_e cannot be varied independently. The data in Figure 2 show that systems of very different C_∞ have similar G_R if they are diluted so that they have the same entanglement density. We find that diluting gives an approximately linear decrease in both G_R and the entanglement density from PPA. In particular, $G_R \approx (1-f)G_R^0$ where G_R^0 is the undiluted value. Thus it appears that straighter chains have larger G_R primarily because they are more densely entangled.

To our knowledge, all previous simulation studies of strain hardening have employed dihedral (trans/gauche) interactions. Since dihedral interactions are absent from the model employed here, our results show that these interactions are not essential for strain hardening. Angular interactions apparently affect strain hardening only because they control the entanglement density through the equilibrium Kuhn length, and because of their less important effects on density and yield stress.

Effect of Temperature

While both the form of the stress–strain curves shown in Figure 1 and the proportionality between G_R and ρ_e are consistent with entropic elasticity, the temperature dependence is not. Figure 3 shows stress–strain curves for temperatures ranging from near zero to slightly below T_g. At higher temperatures, stress increases monotonically with strain, and exhibits a smooth transition to plastic flow. At low temperatures, the initial elastic response is followed by a clear peak and strain

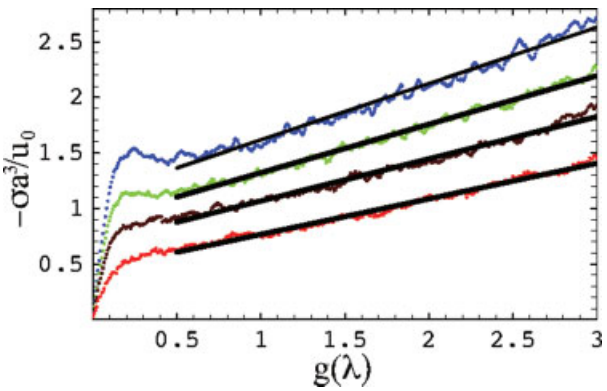

Figure 3. Strain hardening at $k_BT/u_0 = 0.01, 0.1, 0.2,$ and 0.3 from top to bottom. Simulations are done at strain rate $-3.16 \cdot 10^{-4}/\tau_{\text{LJ}}$ with $N_e = 39$, $N_{\text{ch}} = 200$, and $N = 350$. Lines are fits to Gaussian hardening. [Color figure can be viewed in the online issue, which is available at www.interscience.wiley.com.]

Table 2. Temperature Dependence of the Strain Hardening Modulus G_R, Entanglement Density ρ_e, and the Ratios of G_R to the Network Model Prediction and the Flow Stress σ_{flow}

k_BT/u_0	G_Ra^3/u_0	$\rho_e a^3$	$G_R/\rho_e k_BT$	G_R/σ_{flow}
0.01	0.51	0.0134	3800	0.35
0.1	0.44	0.0131	340	0.39
0.2	0.38	0.0129	150	0.41
0.3	0.32	0.0125	85	0.51

Data are for $N_e = 39$ and $\dot{\varepsilon} = -3.16 \cdot 10^{-4}/\tau_{\text{LJ}}$.

softening. In all cases, Gaussian hardening ensues at $g(\lambda) \simeq 0.5$. Again, values of G_R are determined by linear fits to the stress over the range $0.5 \leq g(\lambda) \leq 3$ and are reported in Table 2.

Our results for G_R show a linear decrease over the entire range of T from 0 to $\sim T_g$. A linear decrease was also seen in van Melick et al.'s experiments[7] on increasing T from about $0.6T_g$ to $0.9T_g$. The main difference from our observations is that a greater fractional change in G_R was observed in experiments.[7,15,30] This is due to the high strain rate employed in our simulations. The yield stress and G_R only vanish at T_g in the low strain rate limit. Previous studies in similar systems show that σ_y drops linearly with temperature at all shear rates.[25] At the strain rate used here, σ_y only decreases by about a factor of two as T changes from 0 to T_g. As the strain rate is decreased, σ_y goes to zero at T_g and the fractional change with temperature diverges. The relatively small change in G_R with temperature in Table 2 is consistent with these observations, and rate dependence is discussed further below.

The decrease in G_R with T in experiment[7] and our simulations is inconsistent with entropic network models derived from eq 1. In the simplest form these predict $G_R = \rho_e k_BT$. Experimental and simulation values for both G_R and G_R/ρ_e (Table 2) decrease linearly with increasing T rather than rising linearly. It has been suggested[30,34,36–38] that a drop in effective entanglement density with increasing T could explain a decrease in G_R near T_g. However, in order for a network model to explain the observed monotonic drop in G_R from $T = 0$, the entropy would have to diverge faster than $1/T$ as $T \to 0$, an unlikely proposition. Another difficulty with the network model is that even near T_g the values of G_R are much larger than $\rho_e k_BT$. We find $G_R/\rho_e k_BT$ is of order 100 for $T = 0.2$ and $T = 0.3$, which is similar to the experimental ratios[7] in the same range of T/T_g.

Refs. 15,16 argue that thermally assisted relaxation of the entanglement network is the primary source of the drop in G_R with increasing T. Primitive path analysis does not support this hypothesis. The stretching of primitive paths with strain, $L_{\text{pp}}(\lambda)/L^0_{\text{pp}}$, is the same for $T = 0.3u_0/k_B$ as it is for $T = 0.01u_0/k_B$ ($\sim$1.47 at $\varepsilon = -1.5$). Also, measurements of the nonaffine displacement of atoms as a function of chemical distance from the chain ends indicate that chain end slippage does not occur. Therefore, entanglement loss is negligible, at least at the large strain rate ($\dot{\varepsilon} = -3.16 \cdot 10^{-4}/\tau_{\text{LJ}}$) used in these simulations. Instead, it seems that thermally assisted rearrangement at scales below the entanglement mesh is the primary source of the drop in G_R with increasing T.

Local rearrangements are required to maintain chain connectivity during deformation of the glass. The local stresses required for these rearrangements must be of order of the flow stress. This decreases with increasing T due to thermal activation over local energy barriers (Fig. 3).[25,39,40] The final column in Table 2 gives G_R/σ_{flow}, with σ_{flow} measured at the onset of the strain hardening regime, $g(\lambda) = 0.5$. The ratio of hardening modulus to flow stress changes relatively little over the entire range of T, while $G_R/\rho_e k_BT$ changes dramatically. In the next section we examine the correlation between G_R and σ_{flow} in more detail.

Scaling of G_R with Flow Stress

The most direct way to vary the flow stress is by changing the intermolecular interactions. Changing the strength of the potential u_0 will of course produce proportional increases in G_R and σ_{flow} because all energies scale with u_0. The flow stress also increases when the form of the potential is altered by increasing the cutoff r_c, because a larger region contributes to the energy barriers preventing chains from sliding past each other. Table 3 shows that increasing r_c produces comparable increases in both G_R and σ_{flow}. Their ratio does not change within our numerical uncertainties as they increase by more than 50%. Note that the network model would not predict any change in the configurational entropy or G_R with r_c.

Studies of the strain-rate dependence of the stress also reveal a correlation between G_R and σ_{flow}. Figure 4 shows stress–strain curves for an $N_e = 39$ system at four different strain rates ranging from $-3.16 \cdot 10^{-5}/\tau_{\text{LJ}}$ to $-10^{-3}/\tau_{\text{LJ}}$. The lowest three strain rates show a continuous transition between the elastic regime and plastic flow, while

Table 3. Variation of Strain Hardening Modulus G_R and Flow Stress σ_{flow} with the Range of Adhesive Interactions r_c for $\dot{\varepsilon} = 3.16 \cdot 10^{-4}/\tau_{\text{LJ}}$, $N = 350$, and $N_e = 39$

r_c/a	$G_R a^3/u_0$	$\sigma_{\text{flow}} a^3/u_0$	G_R/σ_{flow}
1.5	0.38	0.92	0.41
1.8	0.45	0.97	0.46
2.2	0.56	1.25	0.45
2.6	0.60	1.44	0.42

the highest rate shows a slight postyield strain-softening. At all strain rates Gaussian strain hardening is observed for $0.5 \leq g(\lambda) \lesssim 3$. Both G_R and σ_{flow} increase by about 35% with strain rate. The increase in G_R is not accounted for in standard theories of strain hardening,[30,34,36] where G_R depends only on ρ_e and T. However, if G_R scales with σ_{flow}, its rate dependence can be explained in terms of thermally activated local rearrangements.

Experimental[6,41] and theoretical[1,25,40] studies of the yield and flow stresses generally find a logarithmic dependence on deformation rate. The simplest explanation is provided by the Eyring theory of thermal activation over an energy barrier that decreases linearly with stress.[42] As the rate increases, there is less time for thermal activation, and the stress required for flow increases as

$$\sigma_{\text{flow}}(\dot{\varepsilon}) = \sigma_{\text{flow}}(\dot{\varepsilon}_0) + b \ \ln(\dot{\varepsilon}/\dot{\varepsilon}_0), \tag{9}$$

where $\dot{\varepsilon}_0$ is a reference rate, $b \equiv k_B T/V^*$, and V^* is a constant with dimensions of volume. While studies[25,40,43] show that b has a more complex dependence on temperature, the basic logarithmic dependence on rate is quite general. The variations in the flow stress observed in Figure 4 are consistent with these studies.

If the hardening modulus is proportional to the flow stress, then the stress–strain curves should scale as

$$\sigma(\lambda, \dot{\varepsilon}) = F(\lambda)\sigma_{\text{flow}}(\dot{\varepsilon}), \tag{10}$$

where F is a dimensionless function of strain. The stress–strain curves for all rates should collapse onto a universal curve, $F(\lambda)$, when normalized by σ_{flow}. As shown in Figure 5, this approach provides an excellent collapse of our data, particularly for $g(\lambda) \lesssim 3$. There is a small deviation near the yield stress for the highest strain rate that is not surprising because σ_y is known to vary with aging as well as rate, while σ_{flow} only depends on rate.[40,44] We found that data for different r_c could also be collapsed onto the same universal curve. The dashed line in Figure 5 illustrates this for $r_c = 2.6a$ and $\dot{\varepsilon} = 10^{-3}$. The total change in σ_{flow} is a factor of two for the curves collapsed in Figure 5.

We also examined the rate dependence of strain hardening for $N_e = 22$ where the hardening is highly nonlinear. The stress–strain curves at different rates also collapsed when scaled by the flow stress, but on a more nonlinear $F(\lambda)$ because of the greater entanglement. Thus the correlation between strain hardening and the stress required for local rearrangements applies for both Gaussian and Langevin hardening regimes.

Glassy strain hardening has been the subject of many constitutive models.[3,6,15,16,30,34,36,41,45] In all of these, the strain and rate dependence is

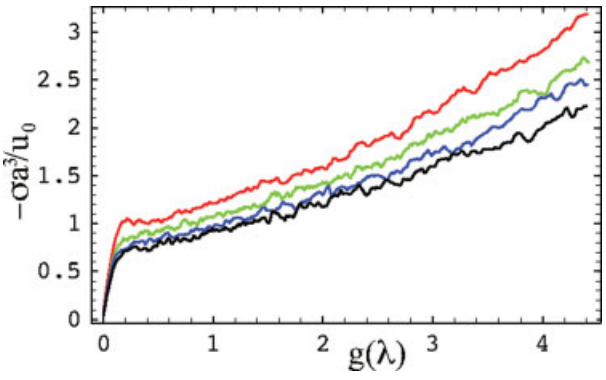

Figure 4. Strain hardening at $\dot{\varepsilon} = -3.16 \cdot 10^{-5}/\tau_{\text{LJ}}$, $-10^{-4}/\tau_{\text{LJ}}$, $-3.16 \cdot 10^{-4}/\tau_{\text{LJ}}$, and $-10^{-3}/\tau_{\text{LJ}}$ from bottom to top. Here $k_B T/u_0 = 0.2$ and $N_e = 39$.

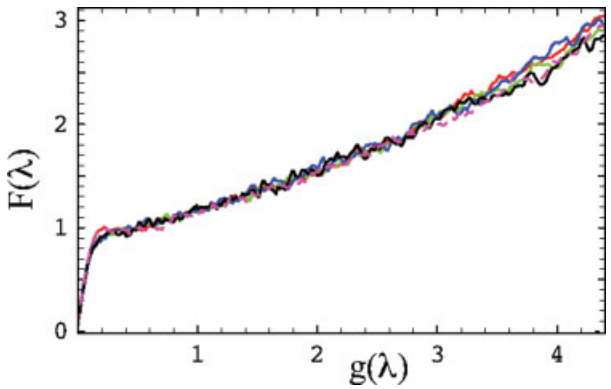

Figure 5. Ratio $F(\lambda)$ of stress to flow stress for the data from Figure 4 with $\dot{\varepsilon} = -3.16 \cdot 10^{-5}/\tau_{\text{LJ}}$ (black), $-10^{-4}/\tau_{\text{LJ}}$ (blue), $-3.16 \cdot 10^{-4}/\tau_{\text{LJ}}$ (green), and $-10^{-3}/\tau_{\text{LJ}}$ (red) with $r_c = 1.5a$. A dashed purple line shows the ratio of stress to flow stress for $r_c = 2.6a$ with $\dot{\varepsilon} = 10^{-3}/\tau_{\text{LJ}}$.

assumed to be additive rather than multiplicative:

$$\sigma(\lambda, \dot{\varepsilon}) = \sigma_1(\lambda) + \sigma_2(\dot{\varepsilon}), \tag{11}$$

where σ_1 and σ_2 represent the nondissipative rubber-elastic stress and viscous stress, respectively. If the stress had this form, the curves in Figure 4 would be shifted vertically by constant offsets and G_R would be independent of deformation rate. The rate dependence of G_R and the collapse of stresses in Figure 5 from the rescaling of eq 10 clearly show that rate-dependent corrections to the stress are multiplicative rather than additive. Note that the correlation of G_R to the flow stress is particularly hard to interpret in rubber elasticity models. These models do not naturally produce a flow stress, and the offset σ_0 in eqs 7 and 8 must be added as an *ad hoc* fitting parameter rather than the central quantity that scales all stresses.

Values of G_R/σ_{flow} in Table 2 increase slightly with temperature, showing a bigger variation than the changes with r_c and rate discussed in this section. This shows that thermally activated relaxation processes reduce σ_{flow} by more than they reduce G_R. One possible explanation is that G_R reflects the local rather than global flow stress, because local rearrangements must occur around each chain to maintain its connectivity during deformation. Studies of the global yield stress show that it decreases with increasing system size because there are more possible sites for fluctuations to nucleate yield.[46] This effect should become more pronounced with increasing temperature, leading to a greater reduction of the large scale flow stress relative to the local flow stress. The rise in G_R/σ_{flow} with increasing T in Table 2 would be reduced if G_R was normalized by a larger local flow stress at higher T.

Chain Length Dependence

Our simulations allow us to test aspects of the microscopic picture underlying the network model. If the effective crosslinks come from entanglements, strain hardening should disappear for $N < N_e$ and saturate for $N \gg N_e$. In addition, the system should deform affinely at scales larger than $\sqrt{\langle R^2(N_e)\rangle}$, something that is difficult to test in experiments.

Figure 6 shows stress–strain curves for undiluted systems with $N_e = 39$ and chain lengths between 4 and 350. The initial elastic response and yield is fairly independent of N, although for large N the yield stress is slightly larger and there is some strain softening. For the $N = 4$ system, yield is followed by perfect-plastic flow, with no strain hardening. All other systems show strain hardening that increases monotonically with N. As expected from the network model, the stress appears to saturate for $N \gg N_e$, and simulations at $N = 500$ showed no further change. Note however that there is a surprisingly large amount of strain hardening even for chains much shorter than the entanglement length. For example, the data for $N = 25$ show linear Gaussian hardening over the entire range of g.

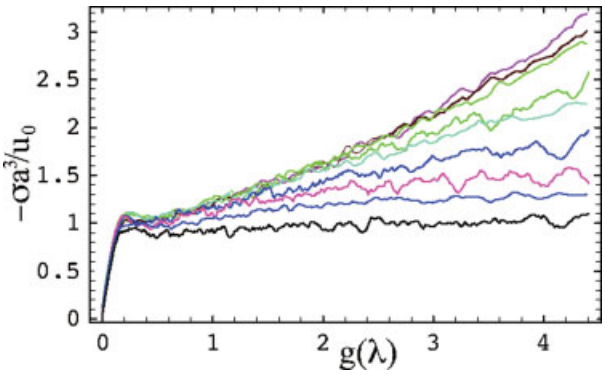

Figure 6. Variation of strain hardening with N for systems with $N_e = 39$ at $k_BT/u_0 = 0.2$ and $\dot{\varepsilon} = -10^{-3}/\tau_{\text{LJ}}$. From bottom to top, $N = 4$, 7, 10, 16, 25, 40, 70, 175 and 350. [Color figure can be viewed in the online issue, which is available at www.interscience.wiley.com.]

Strain hardening can occur as long as there is some order parameter that continues to evolve with increasing strain. We find a correlation between strain hardening and any measure of large scale chain orientation and deformation. A particularly simple one is the rms end to end length as a function of strain $R(\lambda)$ normalized by its value in the initial state ($\lambda = 1$). Figure 7 plots $R(\lambda)/R(1)$ for the systems whose stress–strain curves are depicted in Figure 6. A dashed line shows the prediction for an affine uniaxial deformation at constant volume, $R(\lambda)/R(1) = \sqrt{\lambda^2/3 + 2/3\lambda}$, that is assumed to apply in the Langevin strain hardening model (eq 8).[34] Results for highly entangled chains lie very close to this affine prediction, providing strong evidence that entanglements act like permanent crosslinks during deformation of these glassy systems. The small deviation (~3% for $N = 350$) can be explained by noting that the entanglements will not be at the very ends of the chains and that the segments past the last entanglement need not

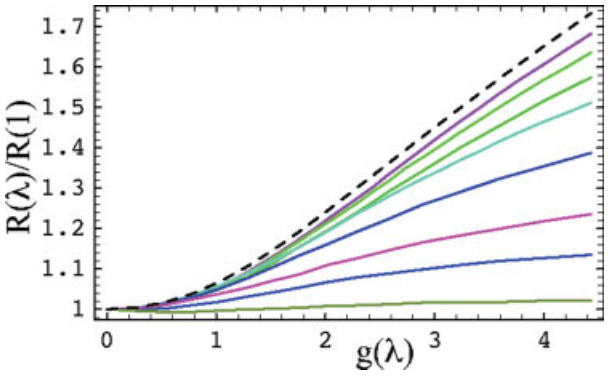

Figure 7. Ratio of total rms length $R(\lambda)$ to unstrained value $R(1)$ as a function of $g(\lambda)$ for $N = 4$, 7, 10, 16, 25, 40, 70, and 350 from bottom to top. A dashed line shows the predicted increase for an affine uniaxial compression at constant volume. Data for $N = 175$ lie on top of the $N = 350$ results and are not shown. Results are for $N_e = 39$ at $\dot{\varepsilon} = -10^{-3}/\tau_{LJ}$. [Color figure can be viewed in the online issue, which is available at www.interscience.wiley.com.]

deform affinely.* Note that neutron scattering experiments on deformed glasses also show that long chains deform nearly affinely on the scale of the radius of gyration, but short chains do not.[47]

There is a clear correlation between the degree of strain hardening (Fig. 6) and that of chain stretching (Fig. 7). The magnitude of the changes in both quantities increases monotonically with N and saturates above 5 to $10N_e$. In this large N limit the chains deform affinely at large scales and their total length becomes irrelevant. Results for shorter chains follow the asymptotic large N behavior at small strains, and then cross over to a less rapid rise at a g that decreases with decreasing N. This suggests that the deformation involves straightening segments of increasing length as g increases. Only when this length becomes comparable to the chain length or N_e do the stress and $R(\lambda)$ begin to saturate or follow the asymptotic behavior.

While chains of length 25 are only 60% of the entanglement length, they remain close to the asymptotic behavior up to $g \approx 2$. Thus for this chain stiffness, entanglements only appear to affect strain hardening for $g > 2$. We expect that the degree of elongation in unentangled systems depends on a competition between the friction preventing relaxation of stretched configurations, and the decreasing number of configurations with a given degree of elongation. Thus the monomer friction, temperature, and strain rate may all affect the value of g where entanglements become important. For example, the higher shear rates used in the simulations of Lyulin et al.[12] may have prevented nonaffine relaxation of short chains, explaining why G_R was essentially the same for entangled and unentangled systems.

The very shortest chains in Figures 6 and 7, $N \leq 10$, lie below the asymptotic curves at all g. The value of $R(1)$ for these chains is already near the completely stretched limit Nl_0 and they cannot align significantly under strain. For example, chains with $N = 4$ (about two Kuhn lengths) start at 80% of their fully extended length and show no strain hardening. For $N = 7$, $R(1)/Nl_0 = 0.6$ and chains only stretch about 10% at the largest g studied.

A recent experimental result[48] is consistent with our observation of strain hardening for chains with $N < N_e$. Wendlandt et al. found that the level of segmental orientation during plastic strain well below T_g is indicative of an effective constraint density much higher than the entanglement density in the melt. In addition to topological entanglements, they postulate the existence of frictional constraints, which cannot relax on the time scale of the experiment. Friction clearly prevents relaxation of the stretching in short chains in our simulations.

Plasticity and Nonaffine Displacements

One measure of the amount of plasticity is the deviation of monomer displacements from an affine deformation:†

$$D^2_{\mathrm{na}} \equiv \langle (\vec{r} - \bar{F}\vec{r}_0)^2 \rangle, \tag{12}$$

where $\bar{F}$ is the macroscopic deformation tensor, $\vec{r}$ is the current position of a given monomer, $\vec{r}_0$ is its initial position at zero strain, and the average is taken over all monomers. To minimize the contributions to D^2_{na} from thermally activated diffusion, we present results for a very low temperature, $k_BT/u_0 = 0.01$. Previous studies have focused on deformation-enhanced mobility at higher temperatures.[11–14]

*Indeed this would predict an error of order N_e/N if the ends did not deform at all. The smaller error observed indicates that the ends also deform substantially. There is also a small correction associated with the change in volume during deformation (~1.3%).

†Small nonaffine deformations accompany elastic deformations in disordered media,[49] but we consider strains well beyond the elastic regime.

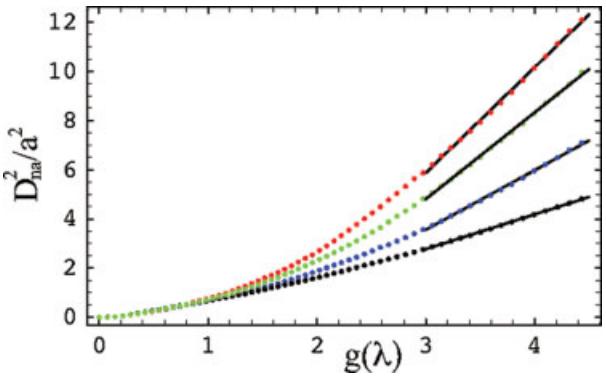

Figure 8. Nonaffine displacement D^2_{na} as a function of $g(\lambda) = 1/\lambda - \lambda^2$. Successive curves from bottom to top are for $N_e = 71$, $N_e = 39$, $N_e = 26$, and $N_e = 22$. Solid lines indicate linear fits to the data for $g(\lambda) \geq 3$. The system parameters are given in Table 1 and the strain rate is $-3.16 \cdot 10^{-4}/\tau_{LJ}$. [Color figure can be viewed in the online issue, which is available at www.interscience.wiley.com.]

Figure 8 shows data for D^2_{na} plotted against $g(\lambda)$ for four different entanglement densities. As noted above, we have also calculated D^2_{na} as a function of the position of atoms along highly entangled chains ($N > 5N_e$). There is no statistically significant variation with position, indicating that chain end slippage does not play an important role.

For strains up to $g(\lambda) \simeq 1$ ($\lambda \simeq 0.7$), the D^2_{na} data fall on a N_e-independent curve, showing that plastic deformation occurs on length scales below the scale of the entanglement mesh. At larger strains, well into the strain hardening regime, the rate of increase of D^2_{na} with $g(\lambda)$ gradually increases, becoming linear in $g(\lambda)$ at large strains. As in plots of stress and other quantities, the increase in the slope of D^2_{na} occurs sooner for lower N_e.

Remarkably, the slopes of D^2_{na} at large strains ($g(\lambda) \geq 3$) are proportional to ρ_e. Table 4 shows values of $(\partial D^2_{na}/\partial g(\lambda))$ obtained from linear fits to D^2_{na} for $g(\lambda) \geq 3$. The fit lines are also shown in Figure 8. Values of $N_e(\partial D^2_{na}/\partial g(\lambda))$ vary by only about 5%. This result is very surprising, especially since the more densely entangled samples are undergoing Langevin hardening at these strains while the hardening in the less entangled samples remains nearly Gaussian. The scaling of D^2_{na} with N_e^{-1} at large g suggests a simple picture in which the amount of plastic deformation is proportional to the density of entanglements.

The increase in stress associated with strain hardening implies that more work must be done to produce each increment in strain. We observe a small increase in energy during deformation that is not expected from the network model, but is much smaller than the work performed. For the systems considered in Figure 8, the percentage of the work that goes into potential energy increases from 8 to 18%, with decreasing N_e. The entropic contribution to the change in free energy is also small, particularly, at the low temperature considered in this section. As a result, most of the work is dissipated as heat following local plastic rearrangements. The rate of work is proportional to the stress and should scale as the rate of plastic rearrangements times the energy dissipated in each.

One way of quantifying the rate of plasticity is to examine the nonaffine deformation δD^2_{na} over a small strain interval $\delta\varepsilon = 0.025$. Another is to count the number of atoms that undergo the large nonaffine displacements associated with plastic events. We find that the two measures are correlated because δD^2_{na} is dominated by the atoms undergoing large displacements with typical size greater than $0.2a$. Both show an increase in plastic deformation with increasing g. There is a rapid rise as the strain approaches the yield point, and then a slower rise in the strain hardening regime. Thus one factor in strain hardening is the increase in the amount of plastic deformation needed to maintain the connectivity of chains as g increases or the degree of entanglement increases. However, it appears that the stress rises more rapidly than the rate of plastic events at large g, particularly for $N_e = 22$. This implies that the energy dissipated in the events is increasing with g. Further studies of plastic deformation are underway.

Primitive Path Statistics

For the systems considered here, the deformation of chains is nearly perfectly affine on the end–end scale and there is negligible disentanglement through chain-end slipping. The network model of entanglements then suggests that the entanglement points and the primitive path between them

Table 4. Slope of Nonaffine Deformation $(\partial D^2_{na}/\partial g(\lambda))$ versus ρ_e

N_e	$(\partial D^2_{na}/\partial g(\lambda))$	$N_e(\partial D^2_{na}/\partial g(\lambda))$
71	1.41	100
39	2.42	94
26	3.52	92
22	4.29	94

Strain rate is $\dot{\varepsilon} = -3.16 \cdot 10^{-4}/\tau_{LJ}$.

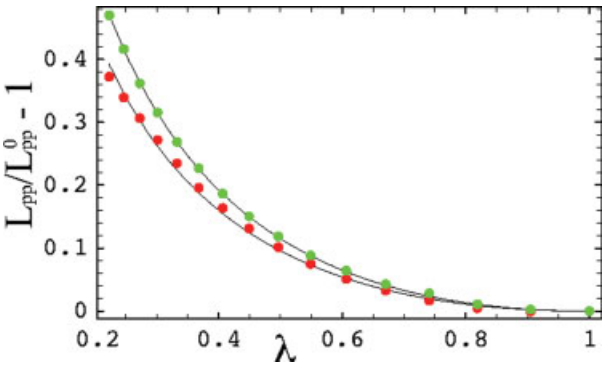

Figure 9. Variation of $L_{pp}(\lambda)/L^0_{pp}-1$ with λ for $N_e = 22$ (bottom) and $N_e = 39$ (top). Solid lines are fits to $c(Y(\lambda)-1)$ with c=0.58 and 0.70, respectively. [Color figure can be viewed in the online issue, which is available at www.interscience.wiley.com.]

will deform affinely. One way of testing this is to compare the increase in the contour length of the primitive path L_{pp} to the network model. Figure 9 shows $L_{pp}(\lambda)/L^0_{pp} - 1$ for $N_e = 22$ and $N_e = 39$. We now show that these results can be described by two seemingly different models.

Affine deformation of the entanglement network implies that the primitive paths should deform affinely at all length scales. We calculate the change in L_{pp} by considering an initial Gaussian path and applying a volume conserving uniaxial compression. Then averaging the change in length over steps with all initial orientations yields:

$$Y(\lambda) \equiv \frac{L^{affine}_{pp}(\lambda)}{L^0_{pp}} = \frac{1}{2}\left(\lambda + \frac{\sin^{-1}(\sqrt{1-\lambda^3})}{\sqrt{\lambda-\lambda^4}}\right). \tag{13}$$

The solid lines in Figure 9 are fits to $c(Y(\lambda) - 1)$, where $c = .58$ for $N_e = 22$ and $c = .70$ for $N_e = 39$. The agreement is excellent, although it is not clear why c is reduced from unity. It appears that there are deviations from affine deformation on the scale of a few monomer spacings. This is insignificant at the scale of an entire chain, but not at the separation of individual entanglements ($\sim 8a$), allowing the primitive path length to stretch less than predicted.

An alternative approach is to calculate the expected evolution of $L_{pp}(\lambda)$ from the nonaffine tube model of Rubinstein and Panyukov.[20] $L_{pp}(\lambda)$ is related to $\langle R^2_{ee}(\lambda)\rangle$ and the strain-dependent tube diameter $a(\lambda)$ by $L_{pp}(\lambda) = \langle R^2_{ee}(\lambda)\rangle/a(\lambda)$. For volume-conserving compression the nonaffine tube model predicts

$$a(\lambda) = \frac{a_0}{\sqrt{3}}\sqrt{\lambda + \frac{2}{\sqrt{\lambda}}}, \tag{14}$$

where a_0 is the tube diameter in the undeformed state. The affinity of the deformation at the end–end scale gives $\langle R^2_{ee}(\lambda)\rangle = (\lambda^2+2/\lambda)\langle R^2_0\rangle$. Replacing $\langle R^2_0\rangle$ with $L^0_{pp}a_0$, a_0 drops out after some algebra, and the prediction is

$$Z(\lambda) = \frac{L_{pp}(\lambda)}{L^0_{pp}} = \frac{1}{\sqrt{3}}\frac{\lambda^2 + 2\lambda^{-1}}{\sqrt{\lambda + 2\lambda^{-1/2}}}. \tag{15}$$

The data in Figure 9 are equally well fit by $d(Z(\lambda) - 1)$, where $d = 0.27$ for $N_e = 22$ and $d = 0.33$ for $N_e = 39$. The reason is that $Z(\lambda)-1 = (35/16)(Y(\lambda)-1)$ to within a few percent over the entire range of λ explored here. The correspondence of $Y(\lambda)$ and $Z(\lambda)$ is somewhat surprising, given the different approaches to their calculation, one coming from a purely mathematical single-chain treatment and the other from a physically motivated mean-field tube model. To the best of our knowledge this has not been previously reported.

CONCLUSIONS

Simulations of strain hardening were carried out for glassy polymer systems with a wide range of entanglement densities. At fixed temperature and strain rate, the results are consistent with the entropic network model. The strain hardening modulus G_R is linearly proportional to the entanglement density ρ_e and does not correlate with chain stiffness alone.[8,9] Both Gaussian and Langevin hardening are observed and the transition between them occurs at the expected entanglement density.

The effect of temperature on strain hardening is in dramatic disagreement with the entropic model. Both G_R and G_R/ρ_e decrease linearly with increasing T rather than being proportional to T. This behavior extends between the $T \to 0$ and $T \to T_g$ limits. To accomodate this behavior, an entropic description would require that S diverge faster than $1/T$ as $T \to 0$. In addition, values of G_R at all temperatures considered were much larger than the entropic prediction $G_R = \rho_e k_B T$. Near T_g the ratio $G_R/\rho_e k_B T$ is of order 100 in both our simulations and recent experiments.[7] The decrease in G_R with increasing T is similar to the corresponding decrease in the flow stress, suggesting

that thermally assisted local rearrangements may reduce both quantities at higher temperatures.

The correlation between G_R and the flow stress extended to variations with interaction parameters and rate. While both G_R and σ_{flow} increase with the strength and range of adhesive interactions, the ratio G_R/σ_{flow} remains essentially constant. Correlated increases with strain rate were also observed. Indeed the stress–strain curves for different rates and interactions collapsed onto a universal curve when normalized by σ_{flow}. The observed multiplicative dependence on strain and strain rate (eq 10) is very different than the additive dependence commonly assumed in constitutive laws (eq 11). The experimental literature offers conflicting results on the rate dependence of strain hardening. Some experiments[6,16,39] show rate-dependent hardening, while others[37,50] do not. Most experiments are fit to additive constitutive laws like eq 11, but a multiplicative form like eq 10 has also been employed.[41] In many cases the flow stress may not change by a large enough factor to distinguish between the two forms, but it would be interesting to test the multiplicative relation on a wider set of experimental data.

The effect of chain length on strain hardening was examined over the entire range of chain lengths from unentangled to fully entangled. Significant strain hardening was found in systems with chains much shorter than the topological entanglement length N_e. Hardening occurs as long as chains are able to continuously orient with increasing strain.

The evolution of microscopic quantities inaccessible to experiment was studied. The nonaffine part of the deformation was observed to fall on an N_e-independent curve at strains up to the early part of the strain hardening regime ($g(\lambda) \approx 1$). This suggests that the deformation is restricted to chain segments shorter than N_e at small strains. The onset of a more rapid rise in the deformation moves to lower strains as N_e decreases and at high strains the rise in deformation is proportional to ρ_e. This is consistent with a simple model in which the amount of nonaffine (or plastic) deformation is proportional to the entanglement density. Studies of local plastic rearrangements indicate that strain hardening results from an increase in the amount of local plastic deformation with increasing strain and ρ_e, as well as an increase in the energy scale of rearrangements. Finally, the scaling of the increase in primitive path lengths was found to be consistent with both an affine primitive chain model and a nonaffine tube model, but the absolute values of the increases were smaller than those predicted.

We hope that the connections we have shown between G_R and flow stress provide additional insight into the physics controlling G_R. The flow stress is related to small scale structure and there is a growing understanding of the factors that control it.[25,40,44,46] The success of the network models in explaining the form of strain hardening suggests that entropic arguments may be able to predict the amount of deformation required to maintain chain connectivity, and thus the function $F(\lambda)$ that multiplies σ_{flow}. Combining this approach with models for σ_{flow} may allow strain hardening to be predicted directly from knowledge of the microsopic interchain interactions.

Edward J. Kramer provided the inspiration for this work. Jorg Röttler and Kenneth S. Schweizer provided useful discussions. Gary S. Grest provided the DBH-equilibrated initial states. The simulations in this paper were carried out using the LAMMPS molecular dynamics software (http://www.cs.sandia.gov/~sjplimp/lammps.html). This material is based upon work supported by the National Science Foundation under Grants No. DMR-0454947 and PHY-99-07949.

REFERENCES AND NOTES

1. The Physics of Glassy Polymers, 2nd ed.; Haward, R. N.; Young, R. J. eds.; Chapman and Hall: London, 1997.
2. Treloar, L. R. G. The Physics of Rubber Elasticity; Clarendon Press: Oxford, 1975.
3. Haward, R. N.; Thackray, G. Proc Roy Soc London Ser A 1968, 302, 453.
4. Kramer, E. J. J Polym Sci Part B: Polym Phys 2005, 43, 3369.
5. Cross, A.; Haward, R. N. Polymer 1978, 19, 677.
6. G'Sell, C.; Jonas, J. J. J Mater Sci 1981, 16, 1956.
7. van Melick, H. G. H.; Govaert, L. E.; Meijer, H. E. H. Polymer 2003, 44, 2493.
8. Haward, R. N. Macromolecules 1993, 26, 5860.
9. Mckechnie, J. I.; Haward, R. N.; Brown, D.; Clarke, J. H. R. Macromolecules 1993, 26, 198.
10. Yashiro, K.; Ito, T.; Tomita, Y. Int J Mech Sci 2003, 45, 1863.
11. Lyulin, A. V.; Balabaev, N. K.; Mazo, M. A.; Michels, M. A. J. Macromolecules 2004, 37, 8785.
12. Lyulin, A. V.; Vorselaars, B.; Mazo, M. A.; Balabaev, N. K.; Michels, M. A. J. Europhys Lett 2005, 71, 618.
13. Capaldi, F. M.; Boyce, M. C.; Rutledge, G. C. Phys Rev Lett 2002, 89, 175505.
14. Capaldi, F. M.; Boyce, M. C.; Rutledge, G. C. Polymer 2004, 45, 1391.

15. Govaert, L. E.; Tervoort, T. A. J Polym Sci Part B: Polym Phys 2004, 42, 2041.
16. Wendlandt, M.; Tervoort, T. A.; Suter, U. W. Polymer 2005, 46, 11786.
17. Kremer, K.; Grest, G. S. J Chem Phys 1990, 92, 5057.
18. Everaers, R.; Sukumaran, S. K.; Grest, G. S.; Svaneborg, C.; Sivasubramanian, A.; Kremer, K. Science 2004, 303, 823.
19. Doi, M.; Edwards, S. F. The Theory of Polymer Dynamics; Clarendon Press: Oxford, 1988.
20. Rubinstein, M.; Panyukov, S. Macromolecules 1997, 30, 8036.
21. Auhl, R.; Everarers, R.; Grest, G. S.; Kremer, K.; Plimpton, S. J. J Chem Phys 2003, 119, 12718.
22. Faller, R.; Kolb, A.; Müller-Plathe, F. Phys Chem Chem Phys 1999, 1, 2071.
23. Frenkel, D.; Smit, B. Understanding Molecular Simulations, 2nd ed.; Academic Press: San Diego, 2002.
24. Schneider, T.; Stoll, E. Phys Rev B 1978, 17, 1302.
25. Rottler, J.; Robbins, M. O. Phys Rev E 2003, 68, 011507.
26. Karayiannis, N. C.; Mavrantzas, V. G.; Theodorou, D. N. Phys Rev Lett 2002, 88, 105503.
27. Hoy, R. S.; Robbins, M. O. Phys Rev E 2005, 72, 061802.
28. Zhou, Q.; Larson, R. G. Macromolecules 2005, 38, 5761.
29. Sukumaran, S. K.; Grest, G. S.; Kremer, K.; Everaers, R. J Polym Sci Part B: Polym Phys 2005, 43, 917.
30. Arruda, E. M.; Boyce, M. C.; Jayachandran, R. Mech Mat 1995, 19, 193.
31. Bartczak, Z. Macromolecules 2005, 38, 7702.
32. Yang, L.; Srolovitz, D. J.; Yee, A. F. J Chem Phys 1997, 107, 4396.
33. Wang, M. C.; Guth, E. J Chem Phys 1952, 20, 1144.
34. Arruda, E. M.; Boyce, M. C. J Mech Phys Solids 1993, 41, 389.
35. Tervoort, T. A.; Govaert, L. E. J Rheology 2000, 44, 1263.
36. Boyce, M. C.; Parks, D. M.; Argon, A. S. Mech Mat 1988, 7, 15.
37. Boyce, M. C.; Arruda, E. M. Polym Eng Sci 1990, 30, 1288.
38. Arruda, E. M.; Boyce, M. C. Int J Plasticity 1993, 9, 697.
39. Hope, P. S.; Ward, I. M.; Gibson, A. G. J Mater Sci 1980, 15, 2207.
40. Rottler, J.; Robbins, M. O. Phys Rev Lett 2005, 95, 225504.
41. G'sell C.; Jonas, J. J. J Mater Sci 1979, 14, 583.
42. Eyring, H. J Chem Phys 1936, 4, 283.
43. Cook, W. D.; Mayr, A. E.; Edward, G. H. Polymer 1998, 39, 3725.
44. Varnik, F.; Bocquet, L.; Barrat, J.-L. J Chem Phys 2004, 120, 2788.
45. Klompen, E. T. J.; Engels, T. A. P.; Govaert, L. E.; Meijer, H. E. H. Macromolecules 2006, 38, 6997.
46. Rottler, J.; Robbins, M. O. Phys Rev E 2001, 64, 051801.
47. Dettenmaier, M.; Maconnachie, A.; Higgins, J. S.; Kaush, H. H.; Nguyen, T. Q. Macromolecules 1986, 19, 773.
48. Wendlandt, M.; Tervoort, T. A.; van Beek, J. D.; Suter, U. W. J Mech Phys Solids 2006, 54, 589.
49. Tanguy, A.; Wittmer, J. P.; Leonforte, F.; Barrat, J.-L. Phys Rev B 2002, 66, 174205.
50. G'Sell, C.; Hiver, J. M.; Dahoun, A.; Souahi, A.; J Mater Sci 1992, 27, 5031.